Cooperative Current Region Control Strategy With Full Speed Range of the Flux-Torque Regulation Hybrid Excitation Machine

Hongbo Qiu, Qimin Wu, Wenbo Chen, and Dongxue Fu

***Abstract*—Due to the inherent characteristics of single-phase (SP) excitation system, it is difficult for flux-torque regulation hybrid excitation machine (FTRHEM) to balance efficiency and torque performance. Therefore, a cooperative current region control strategy with full speed range is proposed in this article. First, a dual *d–q* mathematical model for FTRHEM is established by adopting virtual orthogonal vector to reveal the relationship between flux and torque regulation in SP excitation system. Then, based the speed and torque, the full speed range is divided into constant torque region (modes I and II) and constant power region (modes III and IV). In constant torque region, to improve the efficiency, a maximum torque per ampere control of the armature and excitation currents is designed by the Lagrange multiplier method. In constant power region, considering the voltage capacity of the inverter, an armature-excitation hybrid flux-weakening angle control method is developed by analyzing the voltage and current trajectory to balance efficiency and torque. Finally, the effectiveness of the control strategy is verified by simulation and experiment.**

***Index Terms*—Constant power region, constant torque region, current region control, flux-torque regulation, maximum torque per ampere (MTPA) control.**

I. Introduction

PERMANENT magnet synchronous motor (PMSM) has the advantages of high efficiency, high torque density and high dynamic performance [1], [2], [3], and has been widely used in transportation, aerospace and other fields [4], [5]. However, due to the inherent characteristics of permanent magnet (PM), the air gap field of PMSM is difficult to regulate, the flux weakening control performance is poor, and the constant power operating range is narrow [6]. Hybrid excitation motor (HEM) not only retains the advantages of PMSM, but also has the good flux regulation ability of electric excitation motor [7], [8], [9], [10]. Therefore, some experts and scholars have carried out in-depth research on HEMs in motor topology and control strategy.

For the motor topology, according to the different excitation sources, the HEMs can be divided into direct current (dc) HEMs and alternating current (ac) HEMs. Literature [11] and [12] introduce several typical dc-HEMs with simple structures, but they decrease the ability of torque output in the flux weakening process, operation efficiency and utilization rate of PM [13]. Different from dc-HEMs, Wang et al. [14] proposes a HEM with an independent ac excitation port, which improves the utilization rate of PM flux and end leakage flux by accurately controlling the excitation current. A radial-axial brushless HEM is proposed in [15] by using double-stator partition windings and alternating-pole rotor, which lead flux regulation simple and flexible. Compared with the HEMs with three-phase ac excitation system mentioned in [14] and [15], the excitation system of the flux-torque regulation hybrid excitation machine (FTRHEM) studied in this article adopts single-phase (SP) ac [16], [17], which is not only simpler in structure, but also can realize simultaneous regulation of flux and output torque.

In terms of control strategy, compared with the traditional PMSMs, the HEMs introduce excitation current as an additional control variable, forming a dual-degree of freedom coordinated control system with armature and excitation current that significantly enhances control flexibility. Gu et al. [18] proposes a current control strategy with auxiliary winding for an axial-parallel HEM. The phase voltage amplitude suppression is achieved by leveraging the coupling effect between auxiliary winding and PM flux, thereby reducing both excitation and armature current. However, this approach increases the complexity of drive circuit topology due to the additional auxiliary winding. Pothi et al. [19] establishes a coordinated control model for copper loss minimization in hybrid excitation double salient machines, while literature [20] develops an optimal control algorithm for maximum torque per copper loss (MTPCL) in hybrid excitation flux switching machines. Both studies of [19], [20] improve energy efficiency through optimized allocation of armature and excitation currents. Nevertheless, existing research primarily focuses on dc-HEMs, with insufficient systematic investigation into dynamic control strategies for ac-HEMs.

For ac-HEM drive systems, the control method becomes inherently complex due to the requirement of dual inverters in its topology configuration. In existing research, literature [21] proposes a dc-biased maximum torque per ampere (MTPA)

Received 8 April 2025; revised 21 July 2025; accepted 5 September 2025. Date of publication 10 September 2025; date of current version 22 October 2025. This work was supported in part by Natural Science Foundation of Henan under Grant 232300421070, in part by the National Natural Science Foundation of China under Grant 52477066 and Grant 52177063, and in part by the Program for Science and Technology Innovation Talents in Universities of Henan Province under Grant 23HASTIT026, in part by the Science and technology project of Henan Province under Grant 232102220080, and Grant 242102221002, and in part by Henan Natural Science Foundation Youth Foundation under Project 242300420363. Recommended for publication by Associate Editor J. Dong. *(Corresponding author: Wenbo Chen.)*

The authors are with the Zhengzhou University of Light Industry, Zhengzhou 450000, China. (e-mail: qiuhongbo@zzuli.edu.cn; 332301010009@zzuli.edu.cn; cccwb@zzuli.edu.cn; dongxuefu@zzuli.edu.cn).

Color versions of one or more figures in this article are available at https://doi.org/10.1109/TPEL.2025.3608355.

Digital Object Identifier 10.1109/TPEL.2025.3608355

control strategy that employs polynomial fitting to model optimal operating points derived from experimental data. However, this approach neglects the nonlinear inductance characteristic caused by magnetic saturation, compromising global optimality under varying current ratio conditions. An MTPCL control strategy based on flux coordination for ac-HEMs is developed in literature [22]. This method develops the correlation between inductance parameters and torque characteristics, achieving optimal current selection through combinatorial enumeration. Wang et al. [23] introduces a region control strategy that optimizes current parameters in partitioned operating regions to ensure global optimization. Notably, these methods primarily target three phase ac flux regulation HEM architectures and demonstrate limited applicability to SP-ac flux regulation.

To achieve optimal control performance for HEMs, this article proposes a full speed range current region control strategy for an FTRHEM with SP-ac excitation system, and establishes a mathematical model of FTRHEM based on virtual orthogonal vectors. The main contributions of this article are summarized as follows.

1) A high-precision mathematical model of the FTRHEM is established by introducing virtual orthogonal vectors combined with SP ac flux regulation principle.
2) Based on the characteristics of the developed mathematical model, a full speed range current region control strategy is proposed to further enhance efficiency.
3) A three-dimensional current vector trajectory model is constructed through systematic analysis of current-voltage interactions in armature/excitation dual-winding systems, which enhances visualization and operational feasibility of the control process.

The rest of this article is arranged as follows. In Section II, the topological structure of FTRHEM is introduced, and the mechanism of ac flux regulation and additional torque due to axial excitation generation is explained. In Section III, the radial-axial dual d–q mathematical model of FTRHEM is established. In Section IV, the full speed range of FTRHEM is divided into four operation states, and the corresponding control strategy is given in detail. Section V verifies the effectiveness of the theoretical analysis and the proposed strategy through simulation and experiment. Finally, Section VI concludes this article.

II. Topology and Operating Principle

A. Topological Structure and Principle of Magnetic Modulation

The topology of FTRHEM is shown in Fig. 1. It includes a radial PM component and an axial electric excitation component. Similar to traditional PMSM, the radial PM part contains stator, armature winding and rotor with PMs. The axial electric excitation component fixed at the end cap consists of two sets of inner ferromagnetic ring, outer ferromagnetic ring, and excitation winding. Each inner ferromagnetic ring and outer ferromagnetic ring contain five claw poles, which are alternate arrangements. To match the claw pole, the PMs in rotor are adopted to tangential arrangement, which can generate larger magnetic flux compared

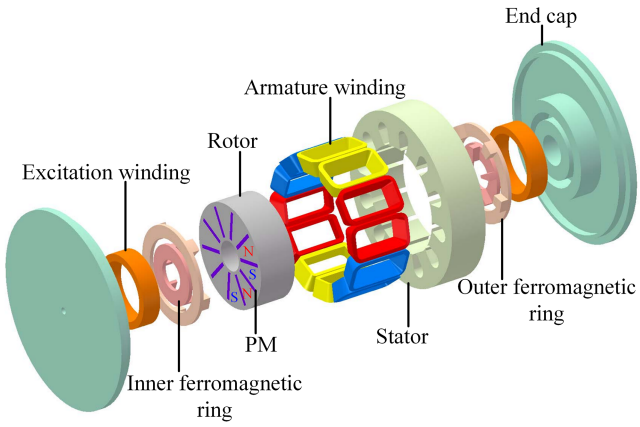

Fig. 1. Topology of FTRHEM.

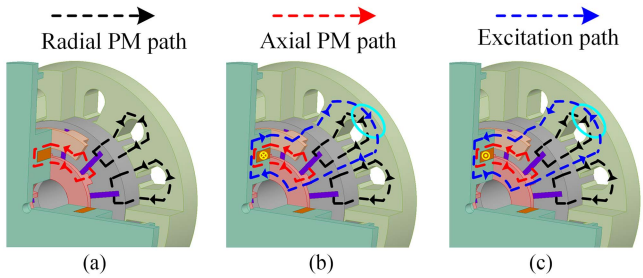

Fig. 2. Flux regulation schematic diagram of FTRHEM. (a) Only PM. (b) Flux enhancing. (c) Flux weakening.

with radial arrangement. In addition, the armature winding and the axial excitation winding are independent of each other and can be controlled by two independent inverters respectively. Furthermore, the structure realizes the parallel connection between the radial PM flux loop and the axial PM flux loop, reducing the risk of demagnetization of the PM in the process of axial flux regulation.

Fig. 2 describes the principle of flux regulation. In Fig. 2(a), the axial and radial air gap flux are only provided by the PMs when the axial part is not working. The red dotted line and black dotted line represent the axial PM path and radial PM path, respectively. Otherwise, the air gap flux is provided by the PMs and excitation current, and the blue dotted line is the excitation path. As shown in Fig. 2(b), FTRHEM is in the state of flux enhancing when the excitation flux is the same direction as radial PM flux. Conversely, when the excitation flux is opposite to the radial PM direction, as shown in Fig. 2(c), FTRHEM is in the state of flux weakening.

B. Additional Torque Due to Axial Excitation

Similar to the operation principle of SP-PMSM [24], [25], the additional torque due to axial excitation of FTRHEM is generated by the interaction between the magnetic flux generated by the axial excitation winding and the axial PM flux. When the positive current is passed into the excitation winding, the S pole and N pole magnetic fields are induced by the inner and

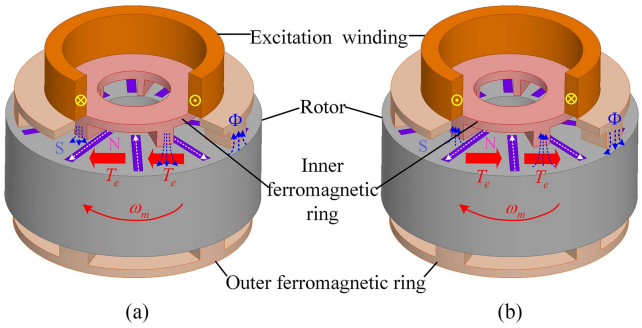

Fig. 3. Schematic diagram of additional torque due to axial excitation. (a) Driving mode. (b) Braking mode.

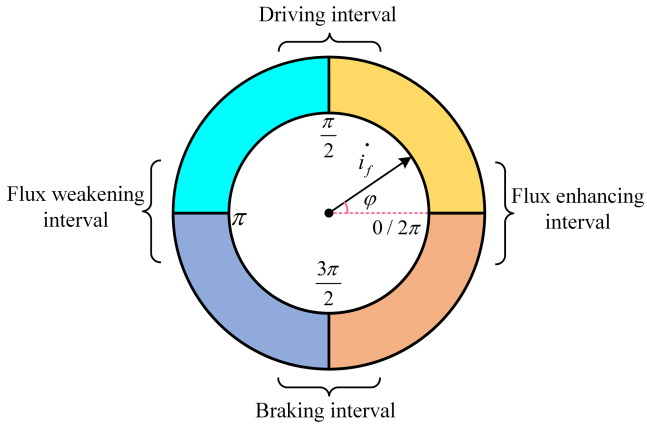

Fig. 4. Properties of phase angle of excitation current.

outer ferromagnetic rings respectively, and the direction of the additional torque generated is the same as that of the motor rotation, which calls the driving mode, as shown in Fig. 3(a). Conversely, the direction of the additional torque is opposite to the direction of the motor rotation, which is called the braking mode, as shown in Fig. 3(b).

III. Mathematical Model of FTRHEM

Due to the FTRHEM excitation flux in excitation winding flows into the radial part through the inner and outer ferromagnetic rings, it is the same as the flux generated by the PM, and can be equivalent to an independent magnetomotive force, so the self-inductance of the excitation winding is not affected by the rotor position [26]. The regulating ability is affected by the mutual inductance between the excitation winding and the armature winding, and its expression is

$$\begin{cases} M_{af} = M_{sf}\cos(\theta_e) \\ M_{bf} = M_{sf}\cos(\theta_e - 120^\circ) \\ M_{cf} = M_{sf}\cos(\theta_e + 120^\circ) \end{cases} \tag{1}$$

where M_{af}, M_{bf}, and M_{cf} are the mutual inductance amplitude between the excitation winding and the armature windings of A-, B-, C-phase, and M_{sf} is the mutual inductance amplitude, θ_e is the electrical angle value of the rotor position.

The three-phase mathematical model of FTRHEM in the stationary coordinate system and the coupling between armature currents are complicated, which make it difficult to design the control system. To solve this problem, the three-phase flux linkage in the stationary coordinate system is transformed into the *d–q* rotating coordinate system by coordinate transformation. However, SP excitation current, due to the lack of a degree of freedom, cannot be directly converted into the *d–q* rotating coordinate system. In this article, the *d–q* rotating transformation of SP is realized by constructing a virtual orthogonal variable of excitation current through second-order general integrator (SOGI) [27], [28].

Assuming the static excitation current is

$$i_\alpha = I_m\cos(\theta_e + \varphi). \tag{2}$$

In an ideal case, the virtual current for the coordinate transformation would be

$$i_\beta = I_m\sin(\theta_e + \varphi) \tag{3}$$

where I_m and φ represent the amplitude and phase of the excitation current, respectively.

Through the coordinate transformation matrix $T_{\alpha\beta/\mathrm{dq}}$, the current component of the excitation current in the *d–q* coordinate system is

$$\begin{bmatrix} i_{df} \\ i_{qf} \end{bmatrix} = T_{\alpha\beta/dq}\begin{bmatrix} i_a \\ i_\beta \end{bmatrix} = \begin{bmatrix} I_\mathrm{m}\cos(\varphi) \\ I_\mathrm{m}\sin(\varphi) \end{bmatrix} \tag{4}$$

$$T_{\alpha\beta/dq} = \begin{bmatrix} \cos(\theta_e) & \sin(\theta_e) \\ -\sin(\theta_e) & \cos(\theta_e) \end{bmatrix}. \tag{5}$$

The operational characteristics of the FTRHEM are systematically analyzed as a function of the excitation current phase angle, as illustrated in Fig. 4. The FTRHEM exhibits distinct operational modes within specific phase angle intervals

1) $\varphi \in (0, \pi/2)$: Enhance flux and torque simultaneously.
2) $\varphi \in (\pi/2, \pi)$: Enhance flux and weaken torque simultaneously.
3) $\varphi \in (\pi, 3\pi/2)$: Weaken flux and torque simultaneously.
4) $\varphi \in (3\pi/2, 2\pi)$: Weaken flux and enhance torque simultaneously.

Furthermore, a critical tradeoff between flux and torque regulation capabilities is observed: the flux regulation capability attains its maximum value when the torque regulation capability is minimized, and vice versa.

On the basis, the flux linkage equation of FTRHEM can be established in dual *d-q* coordinate system as

$$\begin{bmatrix} \psi_d \\ \psi_q \\ \psi_{da} \\ \psi_{qa} \end{bmatrix} = \begin{bmatrix} L_d & 0 & M_{sf} & 0 \\ 0 & L_q & 0 & 0 \\ 1.5M_{sf} & 0 & L_{df} & 0 \\ 0 & 0 & 0 & L_{qf} \end{bmatrix}\begin{bmatrix} i_d \\ i_q \\ i_{df} \\ i_{qf} \end{bmatrix} + \begin{bmatrix} \psi_{pr} \\ 0 \\ \psi_{pa} \\ 0 \end{bmatrix} \tag{6}$$

where ψ_d, ψ_q, ψ_{df}, and ψ_{qf}represent the *d-q* axis flux linkage of the radial and axial air gap respectively. $\psi_{pr}$and ψ_{pa}represent the radial and axial components of PM flux linkage, respectively.

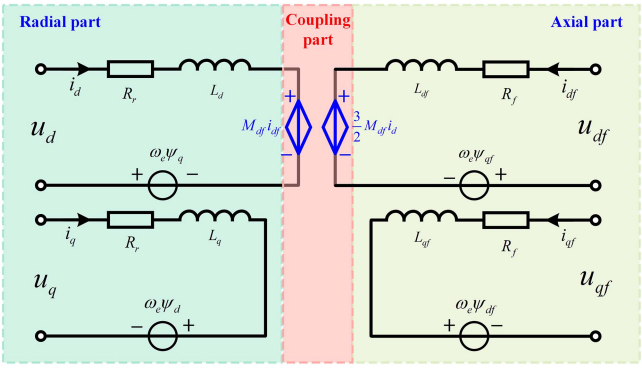

Fig. 5. Equivalent circuit model of FTRHEM.

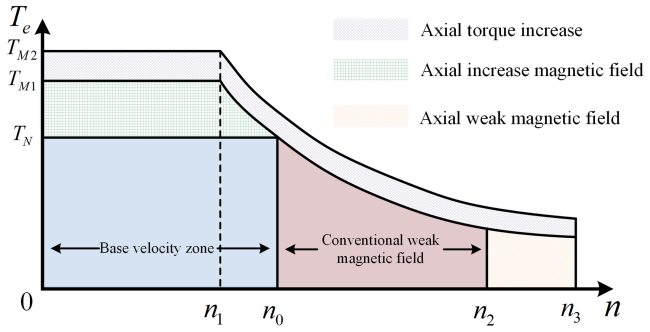

Fig. 6. Working region and operation modes of FTRHEM.

L_d, L_q, L_{df}, L_{qf}, i_d, i_q, i_{df} and i_{qf} respectively represent the d–q axis inductance and current of the radial part and axial part.

Refer to (6), the voltage equation of FTRHEM can be obtained as

$$\boldsymbol{u} = \boldsymbol{P}\cdot\boldsymbol{i} + \boldsymbol{Q}\cdot\dot{\boldsymbol{i}} + \boldsymbol{N} \tag{7}$$

where $\boldsymbol{P} = \begin{bmatrix} R_r & -\omega_e L_q & 0 & 0 \\ \omega_e L_d & R_r & \omega_e M_{sf} & 0 \\ 0 & 0 & R_f & -\omega_e L_{qf} \\ 1.5\omega_e M_{sf} & 0 & \omega_e L_{df} & R_f \end{bmatrix}$,

$\boldsymbol{Q} = \begin{bmatrix} L_d & 0 & M_{sf} & 0 \\ 0 & L_q & 0 & 0 \\ 1.5M_{sf} & 0 & L_{df} & 0 \\ 0 & 0 & 0 & L_{qf} \end{bmatrix}$, $\boldsymbol{u} = \begin{bmatrix} u_d \\ u_q \\ u_{df} \\ u_{qf} \end{bmatrix}$, $\boldsymbol{i} = \begin{bmatrix} i_d \\ i_q \\ i_{df} \\ i_{qf} \end{bmatrix}$,

$\mathbf{N} = \begin{bmatrix} 0 \\ \omega_e\psi_{pr} \\ 0 \\ \omega_e\psi_{pa} \end{bmatrix}$, u_d, u_q, u_{df} and u_{qf} represent the radial and axial d–q axis voltage, respectively; R_r, R_f, and ω_e represent the resistance of the radial winding and axial coil and the electrical angular velocity of the rotor, respectively.

Since the self-inductance of the excitation winding is not affected by the rotor position, it follows that the d-axis inductance is equal to the q-axis inductance, i.e., $L_{df} = L_{qf}$. And the electromagnetic torque equation of FTRHEM can be expressed as

$$\begin{aligned} T_e = {} & \tfrac{3P}{2}\left[\left(\psi_{pr} + M_{sf}i_{df}\right)i_q + \left(L_d - L_q\right)i_d i_q\right] \\ & + P\left(\psi_{pa} + \tfrac{3}{2}M_{sf}i_d\right)i_{qf} \end{aligned} \tag{8}$$

where T_e is the electromagnetic torque and P is the number of pole pairs of the motor.

Refer to (7), the equivalent circuit model of FTRHEM is illustrated in Fig. 5, which indicates that the radial part and the axial part only have a coupling relationship on the d-axis, and do not affect each other on the q-axis.

IV. Current Region Control Strategy

It can be seen from the above model of flux linkage and torque that the excitation current of FTRHEM can not only regulate the flux, but also control the additional torque due to axial excitation to change the torque output. Compared with traditional PMSM and dc HEM, FTRHEM has a larger working region, which is given in Fig. 6. On the basis, the full speed range is divided into the following four operation modes.

Mode I: $0{\sim}n_1\&0{\sim}T_{M2}\|0{\sim}n_0\&0{\sim}T_N$. When the motor works within the rated speed range, the voltage capacity of the inverter is sufficient, and only the current capacity needs to be considered. For FTRHEM, in addition to the armature current to provide the main torque output, the excitation current can improve torque output performance through the additional torque and the flux enhancing.

Mode II: $n_1{\sim}n_0\&T_N{\sim}T_{M2}$. When the high torque state within the rated speed range, both the voltage capacity of the inverter and the current capacity needs to be considered. With the increase of speed, the d-axis component of excitation current becomes smaller, until it decreases to 0.

Mode III: $n_0{\sim}n_2$. In the high-speed range, the voltage capacity of the inverter has reached saturation. FTRHEM can weak air gap flux by increasing d-axial component of the armature current and excitation current to improve the speed. Furthermore, the additional torque can improve torque output performance.

Mode IV: $n_2{\sim}n_3$. When FTRHEM works in the ultra-high-speed range, the voltage capacity and current capacity of the inverter in radial part are saturated. For the axial part, the excitation current needs to further increase the d-axial component, and the q-axial component will gradually decrease in the meantime, until it decreases to 0.

According to the speed and load of FTRHEM, the current region control strategy is shown in Fig. 7.

A. Constant Torque Control Strategy

The constant torque region (mode I and mode II) is the low-speed range. In mode I, to minimize the amplitude of the current vector required when the output torque is constant, and reduce the operation loss, this article presents a new MTPA control method for FTRHEM. Due to the light load, there is no need to consider the current capacity, so constraint condition is the torque equation, and the objective function is

$$\min\ i_d^2 + i_q^2 + i_{df}^2 + i_{qf}^2. \tag{9}$$

The Lagrange multiplier method is used to solve the equation, and the Lagrange equation can be obtained by combining (8) and

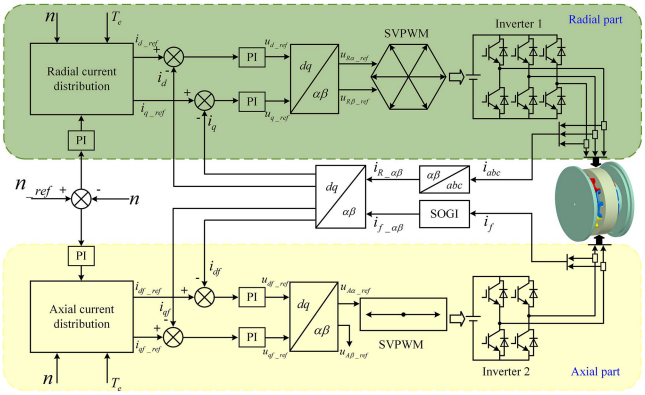

Fig. 7. Current region control strategy of FTRHEM.

(9)

$$L_1 = i_d^2 + i_q^2 + i_{df}^2 + i_{qf}^2 + \lambda \left\{ \begin{array}{c} T_e - \frac{3P}{2}\left[\left(\psi_{pr} + M_{sf} i_{df}\right) i_q + \left(L_d - L_q\right) i_d i_q\right] \\ -P\left(\psi_{pa} + \frac{3}{2} M_{sf} i_d\right) i_{qf} \end{array} \right\} \quad (10)$$

where λ is the Lagrange operator.

Take the partial derivative of each current in (10) and make its partial derivative equal to zero to obtain the extreme point under a certain torque, as shown

$$\frac{\partial L}{\partial i_d} = \frac{\partial L}{\partial i_q} = \frac{\partial L}{\partial i_{df}} = \frac{\partial L}{\partial i_{qf}} = \frac{\partial L}{\partial \lambda} = 0. \quad (11)$$

In mode II, the current capacity of inverter used in armature part reaches saturation. At this time, if MTPA control is to be adopted, the voltage capacity of inverter used in armature part needs to be taken into account, and its constraint conditions are updated as

$$\begin{cases} T_e = \frac{3P}{2}\left[\left(\psi_{pr} + M_{sf} i_{df}\right) i_q + \left(L_d - L_q\right) i_d i_q\right] \\ +P\left(\psi_{pa} + \frac{3}{2} M_{sf} i_d\right) i_{qf} \\ i_d^2 + i_q^2 = i_{r\_\lim}^2 \\ \left(L_q i_q\right)^2 + \left(L_d i_d + M_{df} i_{df} + \psi_{fr}\right)^2 \le \left(\frac{u_{r\_\lim}}{\omega_e}\right)^2 \end{cases}. \quad (12)$$

According to (9) and (12), the Lagrange equation can be obtained as

$$L_2 = i_{r\_\lim}^2 + i_{df}^2 + i_{qf}^2 + \eta \left\{ \begin{array}{c} T_e - \frac{3P}{2}\left[\left(\psi_{pr} + M_{sf} i_{df}\right) i_q + \left(L_d - L_q\right) i_d i_q\right] \\ -P\left(\psi_{pa} + \frac{3}{2} M_{sf} i_d\right) i_{qf} \end{array} \right\} + \kappa \left[\left(L_q i_q\right)^2 + \left(L_d i_d + M_{df} i_{df} + \psi_{fr}\right)^2 - \left(\frac{u_{r\_\lim}}{\omega_e}\right)^2 \right] \quad (13)$$

where η and κ are the Lagrange operator.

Equation (13) can be solved by using the Kuhn–Tucker condition, and the optimal solution of excitation current under a certain torque can be obtained. Combined with the optimal solution of Mode I, the current vector trajectory of FTRHEM in the constant torque region can be obtained, as shown in Fig. 8(a). The starting point of the current trajectory is O, enters the Mode I, falls on

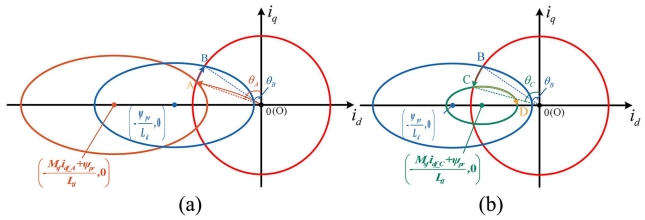

Fig. 8. Armature space current trajectory. (a) Constant torque region. (b) Constant power region.

the current limit circle at point $A(i_{d\_A}, i_{q\_A})$, at which time the flux-weakening angle of the armature current is θ_A, and then runs along the current limit circle to point $B(i_{d\_B}, i_{q\_B})$, at which time the motor runs in the mode II; and the flux-weakening angle is θ_B.

For the SP excitation system, the relationship between excitation voltage and excitation current can be obtained by combining (6)

$$u_f = u_R + u_L + u_{\text{emf}} = R_f i_f + L_f \frac{di_f}{dt} + \omega_e \left(\psi_{pa} + M_{sf} i_d\right) \sin\left(\omega_e t\right). \quad (14)$$

As indicated by (14), the magnitude of the back electromotive force (EMF) varies with rotational speed, while the voltage drops across the resistance and inductance of the excitation winding are governed by the excitation current. As illustrated in Fig. 9, the black dashed circle represents the excitation current limit boundary, the blue dashed circle denotes the excitation voltage limit boundary whose radius is primarily determined by the dc-bus voltage, and the red solid circle indicates the operational boundary of the inverter output voltage trajectory. Since the resistive voltage drop aligns with the current vector in phase, whereas the inductive voltage drop leads the current vector by 90°, the combined loci of these voltage drops can be geometrically represented within a unified circle. The diameter of this synthesized circle is

$$r = \sqrt{\frac{R_f^2 + \left(\omega_e L_f\right)^2}{2}} \cdot I_m. \quad (15)$$

Fig. 9(a) illustrates the output voltage characteristics of the excitation-side inverter during the constant torque operation region of FTRHEM. Taking operating state of point A as a case study, when the excitation current reaches its current limit under MTPA condition, the phase angle of the excitation current vector is determined as

$$\varphi = \arctan\left(\frac{i_{qf}}{i_{df}}\right). \quad (16)$$

The implementation of flux-weakening control through the d-axis armature current component results in a measurable attenuation of the back EMF in the excitation circuit. Furthermore, given the relatively low rotational speed within the constant torque region and the minimal phase angle variation of excitation current during the O-A-B trajectory evolution, the linear path

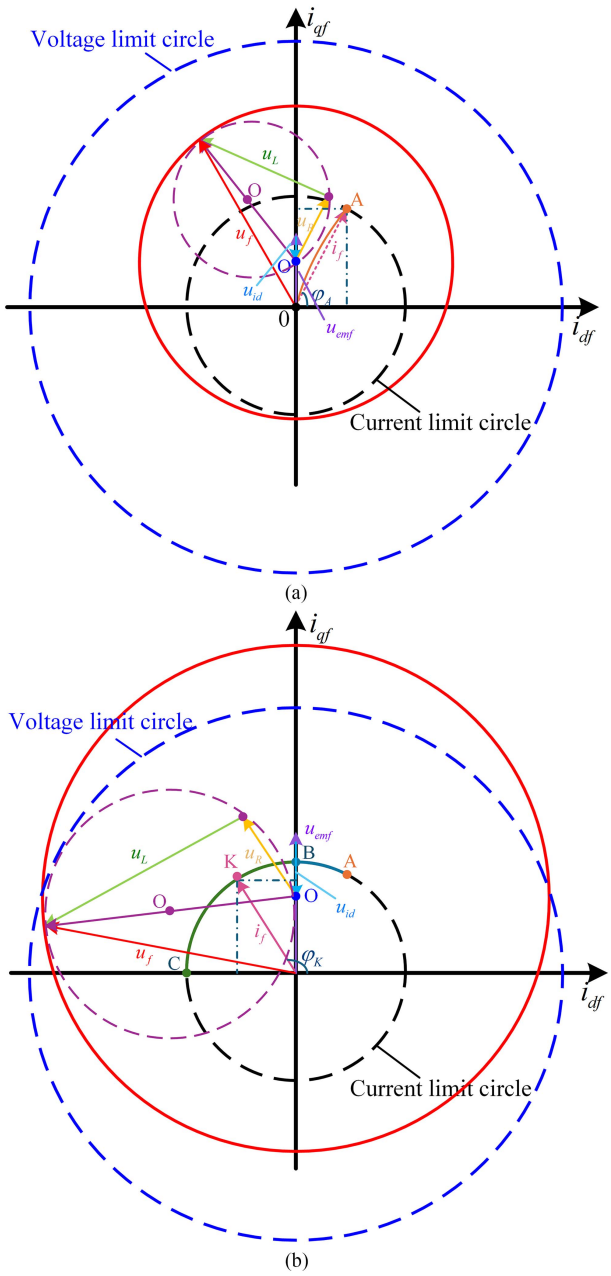

Fig. 9. Inverter output voltage trajectory of excitation component. (a) Constant torque region. (b) Constant power region.

indicated by the red arrow in Fig. 9(a) can be effectively approximated as the operational locus of excitation voltage vector throughout the constant torque operating regime.

B. Constant Power Control Strategy

When the speed exceeds that of point B, the motor enters the constant power region, namely mode III and mode IV. As the back EMF of the FTRHEM increases proportionally with speed, flux-weakening current becomes necessary to accommodate high-speed operation. In Mode III, to maximum the speed range extension, the excitation current is mainly used for flux weakening, and its torque increasing component is small.

In order to make FTRHEM transition smoothly from the mode II to mode III, the armature current flux-weakening angle θ for interval identification and current distribution control is adopted, and the offset $\Delta\theta$ of flux-weakening angle is calculated using the armature voltage feedback weak magnetic PI controller, whose expression is as follows:

$$\Delta\theta = \left(K_p + \frac{K_i}{s}\right)\left(u_{r\_\lim} - \sqrt{u_d^2 + u_q^2}\right). \tag{17}$$

To make sufficiently use of the current capacity of the inverter in radial part and take the principle of the shortest distance, the two-dimensions (2D) current vector trajectory controlled for mode III is shown in Fig. 8(b), where the starting point is the end point B of MTPA control in the constant torque region, and the end point is the starting point $C(i_{d\_C}, i_{q\_C})$ of the deep weak magnetic field of mode IV.

When the speed is increasing, it will enter the mode III from the operating point *B*, as shown in Fig. 8(b). Due to the insufficient voltage capacity of the inverter in radial part, the flux-weakening angle is updated to $(\theta_B + \Delta\theta)$, and the current expression of FTRHEM in the working area of Mode III is determined by the new flux-weakening angle and the trajectory coordinates of points *B* and *C*

$$\begin{bmatrix} i_d \\ i_q \\ i_{df} \\ i_{qf} \end{bmatrix} = \begin{bmatrix} I_{r\_\max}\sin(\theta_B + \Delta\theta) \\ I_{r\_\max}\cos(\theta_B + \Delta\theta) \\ i_{df\_A} + m\,(\Delta\theta) \\ \sqrt{i_{a\_\lim}^2 - i_{df}^2} \end{bmatrix} \tag{18}$$

where $I_{r\_\max}$ is the maximum current output of the inverter in radial part, $m = (i_{df\_C} - i_{df\_B})/(\theta_C - \theta_B)$.

As illustrated in Fig. 9(b), when the FTRHEM operates in the field-weakening region (trajectory segment *B*-*C*), the excitation current has already reached saturation. Consequently, flux and torque regulation can only be achieved through phase angle adjustment. Taking operating state of point *K* in the field-weakening region as an example: while the excitation current magnitude remains identical to that at point *A*, the phase angle shifts from $\varphi_A$to φ_K. Furthermore, the increased rotational speed elevates both the back EMF and inductive voltage drop, resulting in an expanded radius of the resistance-inductance voltage drop circle. As rotational speed varies during the trajectory segment *B*-*C*, this voltage drop circle undergoes rotational transformation about the back EMF voltage point *O* as its pivotal center.

With the further increase of speed, considering the influence of excitation current, when the center of the radial voltage limit elliptic cylinder is located in the current limit cylinder, the motor is in a deep flux weakening state, that is, FTRHEM operates in mode IV. In order to select the end point of the 2D current trajectory in mode IV, this article adopts the minimum excitation current as the goal to solve and calculate, and the specific expression is as follows:

$$\begin{cases} \min & i_{df}^2 + i_{qf}^2 \\ \text{s.t.} & \psi_{pr} + L_d i_d + M_{sf} i_{df} = 0 \end{cases}. \tag{19}$$

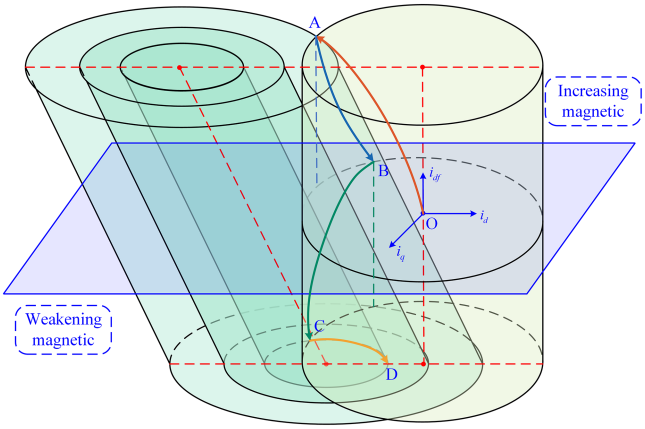

Fig. 10. 3D current vector trajectory.

Refer to (14), the vector coordinates of point C, the start point of the deep flux weakening, can be solved by constructing the Lagrange function

$$\begin{bmatrix} i_{d\_C} \\ i_{q\_C} \\ i_{df\_C} \end{bmatrix} = \begin{bmatrix} -\psi_{pr} L_d / \left(L_d^2 + M_{sf}^2\right) \\ 0 \\ -\psi_{pr} M_{sf} / \left(L_d^2 + M_{sf}^2\right) \end{bmatrix}. \tag{20}$$

In order to make the trajectory of the 2D current vector of FTRHEM smoothly move from point C to point D, the MTPV control based on $i_{df} = i_{df\_D}$ is adopted, whose calculation formula is as follows:

$$\frac{\partial T_e}{\partial i_d} \cdot \frac{\partial u_r}{\partial i_q} - \frac{\partial T_e}{\partial i_q} \cdot \frac{\partial u_r}{\partial i_d} = 0 \tag{21}$$

where $u_r = \sqrt{(\omega_e L_q i_q)^2 + [\omega_e(\psi_{pr} + L_d i_d + M_{sf} i_{df\_D})]^2}$, $i_{qf} = 0$.

By combining (8) and (21), the curve trajectory of MTPV can be obtained as

$$i_d = -\frac{(2L_d - L_q)(\psi_{pa} + M_{sf} i_{df\_C})}{2L_d(L_d - L_q)} + \frac{\sqrt{L_q^2(\psi_{pr} + M_{sf} i_{df\_C})^2 + 4L_q^2(L_d - L_q)^2 i_q^2}}{2L_d(L_d - L_q)}. \tag{22}$$

C. Current Trajectory

To comprehensively investigate the dynamic coupling mechanisms between the SP excitation system and armature windings, this article establishes a three-dimensional current trajectory evolution model for armature-excitation currents in the $i_d - i_q - i_{df}$ orthogonal coordinate system, as illustrated in Fig. 10, based on the FTRHEM full speed range operational characteristic analysis framework.

In the constant torque region (trajectory segment *O-A-B*), the excitation current exhibits continuous flux-torque enhancing behavior, with its phase angle magnitude increasing to the rise in load torque. In the constant power region (trajectory segment *B-C-D*), the phase angle magnitude of the excitation current is predominantly governed by speed. The evolution of the phase angle reveals a progressive switching mechanism in the excitation current, transitioning sequentially from a pure torque enhancing domain to a hybrid flux weakening/torque enhancing control domain, and ultimately entering a full flux weakening operational state.

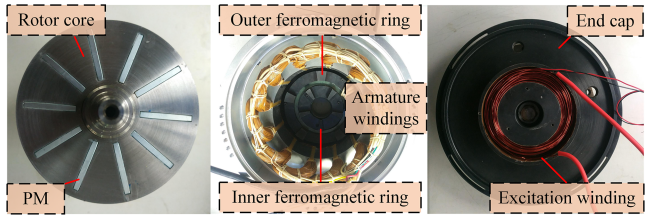

Fig. 11. FTRHEM prototypes.

TABLE I
BASIC PARAMETERS OF FTRHEM PROTOTYPE

Parameters	Value	Parameters	Value
Rated speed (r/min)	250	Rated frequency (Hz)	12
Armature coil turns	175	Excitation coil turns	150
Motor length (mm)	160	Stator slots	12
Shaft diameter (mm)	40	Rotor pole number	10
Stator bore (mm)	140	Length of PM (mm)	40
Stator shaft length (mm)	50	Width of PM (mm)	5
Radial air gap (mm)	0.35	Axial air gap (mm)	0.5

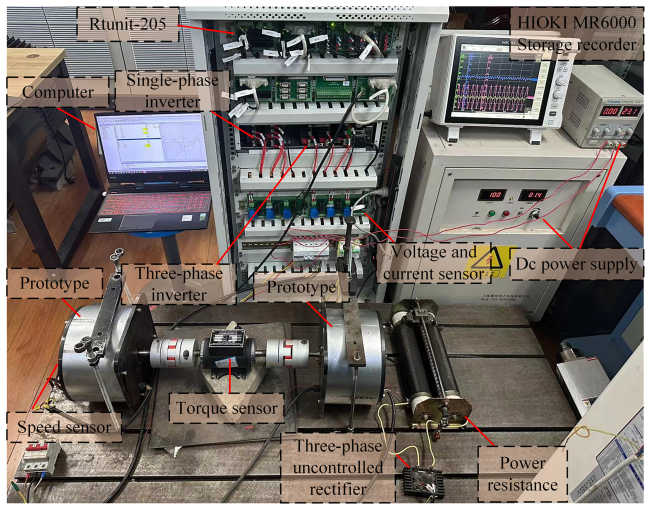

Fig. 12. FTRHEM experiment platform.

V. EXPERIMENT AND SIMULATION

In order to study the performance of FTRHEM and verify the effectiveness of the proposed current region control strategy, a 12 slots/10 poles FTRHEM prototype has been manufactured for experimental verification. Fig. 11 is the FTRHEM prototype, and some basic parameters of FTRHEM prototype are listed in Table I. The simulation is carried out in MATLAB/Simulink, and the experiment is carried out on RTU-BOX205 Real-time controller, as shown in Fig. 12.

The verification is divided into three parts.

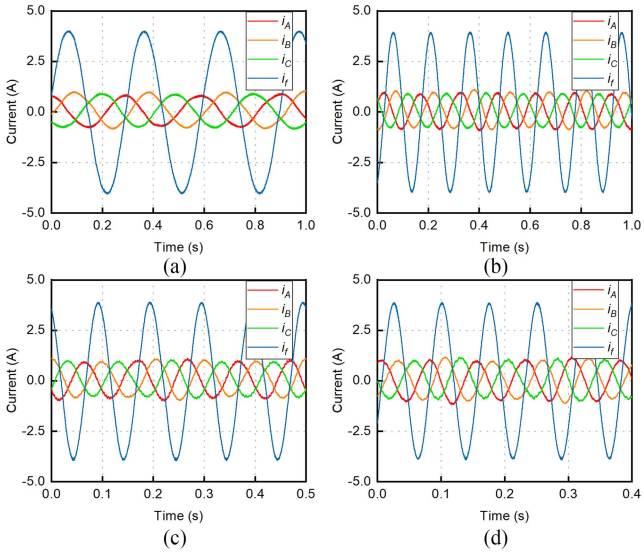

Fig. 13. A-, B-, C-phase and excitation currents of FTRHEM at different speed of 6 N·m load. (a) 40 r/min. (b) 80 r/min. (c) 120 r/min. (d) 160 r/min.

1) Verify the correctness of the FTRHEM model.
2) Verify the effectiveness of the proposed MTPA control strategy in the constant torque region.
3) Verify the effectiveness of the proposed flux weakening control strategy in the constant power region.

The FTRHEM performs loading experiments by dragging a motor connected to a power resistor and is connected to a torque sensor. The RTU-BOX205 Real-time controller connects the radial armature winding through a three-phase full-bridge inverter and the axial excitation winding through a SP full-bridge inverter. The speed and position information are obtained by the incremental encoder.

A. *Dual* D–Q *Mathematical Model Verification*

The waveforms of the A-, B-, C-phase and excitation currents of FTRHEM at different speed are given in Fig. 13. Under the condition of 6 N·m load, the amplitudes of the A-, B-, C-phase and excitation currents basically do not change, showing good sinusoidal characteristics, and the electric frequency of the armature current is the same as that of the excitation current. In addition, from the simulation and experimental results in [17], it can be seen that with the change of the excitation current phase angle, the flux regulation ability and torque regulation ability of FTRHEM change periodically, and the torque regulation ability is the smallest when the flux regulation ability is the largest. The experimental results exhibit excellent agreement with the established dual *d–q* coordinate system mathematical model, thereby validating the accuracy and effectiveness of this model.

B. *Effectiveness of Constant Torque Region Control Strategies*

During experimental operations, the FTRHEM is designed with a rated torque $T_N = 10\ \mathrm{N \cdot m}$, a maximum torque $T_{M2} = 18\ \mathrm{N \cdot m}$, a rated speed $n_0 = 250\ \mathrm{r/min}$ and a maximum speed $n_3 = 400\ \mathrm{r/min}$.

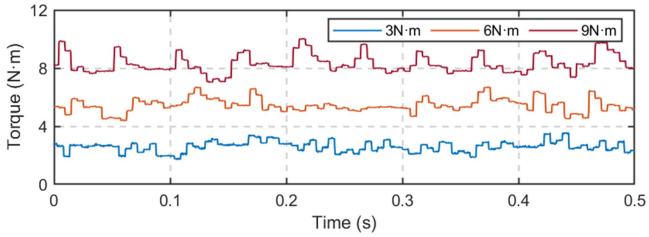

Fig. 14. Output torque of FTRHEM at 3, 6, and 9 N·m loads.

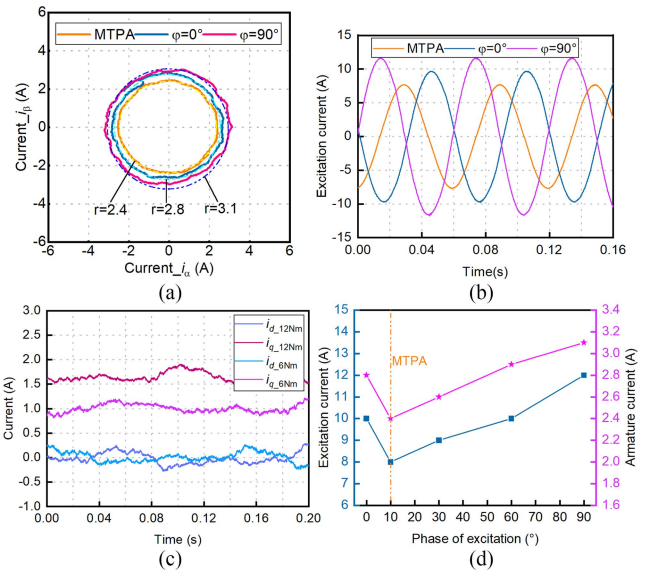

Fig. 15. Change of FTRHEM armature and excitation currents using MTPA, $\varphi = 0°$, $\varphi = 90°$. (a) Armature current of FTRHEM at 200 r/min and 12 N·m. (b) Excitation current of FTRHEM at 200 r/min and 12 N·m. (c) *d–q* current of armature part of FTRHEM at 200 r/min. (d) Relationship between excitation and armature currents of FTRHEM with the phase angle of excitation current at 12 N·m.

In the constant torque region I (Model I operation region), experiments are conducted to evaluate the current characteristics of the FTRIEM under an 6 N·m load at rotational speeds of 40 r/min, 80 r/min, 120 r/min, and 160 r/min, as shown in Fig. 13. The results indicate that both armature current and excitation current exhibit excellent sinusoidal waveforms when voltage and current margins meet operational requirements.

Furthermore, under a speed of 120 r/min, the output torque of the FTRHEM is measured at load conditions of 3, 6, and 9 N·m, as exhibited in Fig. 14. Experimental results demonstrate that the average output torque consistently tracks the target load values of 3, 6, and 9 N·m. However, the torque ripple will sightly increase with escalating load magnitudes.

When the speed increased to 200 r/min and the torque is elevated to 12 N·m, the system entered constant torque region II (mode II operation region). Comparative experiments are performed using three control strategies: MTPA; $\varphi = 0°$; and $\varphi = 90°$, as illustrated in Fig. 15. The experimental data demonstrates that the MTPA method reduces armature current by approximately 15% and excitation current by 20% compared to the

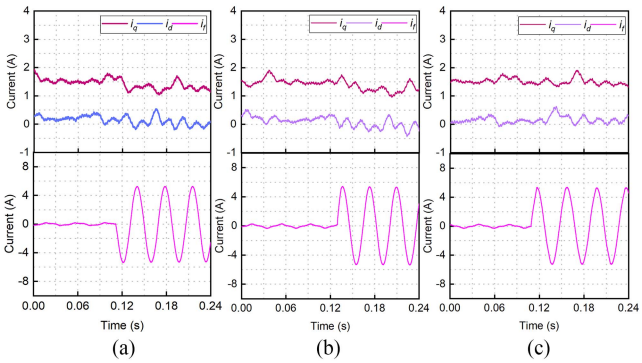

Fig. 16. Change of armature current and excitation in mode III. (a) Proposed method. (b) $\varphi = 0°$. (c) $\varphi = 90°$.

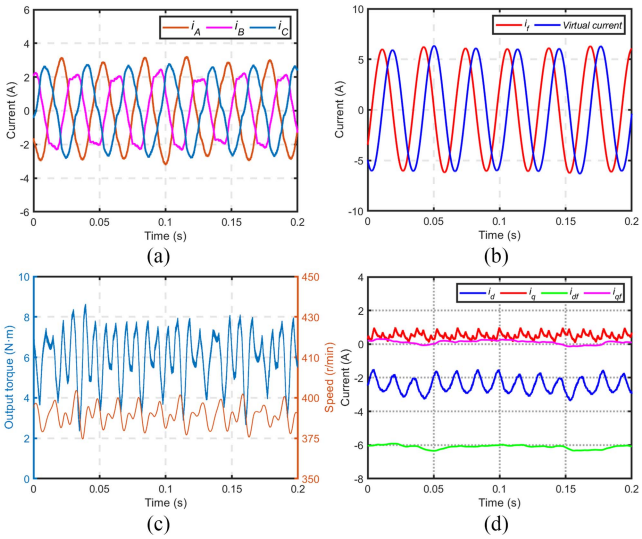

Fig. 17. MTPV control. (a) A-, B-, C-phase current. (b) Excitation current and virtual current. (c) Output torque and speed. (d) Axial and radial d–q axis currents.

$\varphi = 0°$ strategy. Furthermore, relative to the $\varphi = 90°$ method, MTPA achieves reductions of 23% in armature current and 33% in excitation current. Additionally, Fig. 15(a) and (d) reveals that the FTRIEM exhibits significantly stronger torque regulation ability than flux adjustment ability under these conditions.

C. Effectiveness of Constant Power Region Control Strategies

Based on mode II operation, the speed is increased to 300 r/min with the load reduced to 10 N·m, transitioning the system into the constant power region I (mode III operation region). To validate the contribution of excitation current to field-torque coordination and the effectiveness of the proposed method in flux-weakening regions, experiments are conducted to compare the dynamic responses of armature d–q axis currents under three control strategies: the proposed method, $\varphi = 0°$, and$\varphi = 90°$, with excitation current stepped from 0.5 A to 6 A, as shown in Fig. 16. The results demonstrate that all strategies achieve flux-torque coordination via excitation current. However, the $\varphi = 0°$ control exhibits significant q-axis current fluctuations, leading to aggravated torque ripples. While the $\varphi = 90°$ control reduces d–q current oscillations, its sensitivity to excitation current deteriorates markedly. In contrast, the proposed method maintains low current oscillations while preserving effective responsiveness to excitation current variations, demonstrating superior comprehensive performance.

On the basis of mode III, the speed increases to 380 r/min, and the load reduces to 6 N·m. At this time, FTRHEM enters the deep weak magnetic state of mode IV. In Fig. 17, the change of speed and current for MTPV control. Due to the limitation of the voltage and current capacity of the axial inverter, the amplitude of the excitation current is 6 A, and it is basically used for weak magnetic. The amplitude of the armature current is about 2.5 A, and the main part is also used for flux weakening. As shown in Fig. 17(c), the output torque ripple is approximately 2 N·m, and the speed ripple is approximately 10 r/min, with both exhibiting identical fluctuation frequencies.

VI. Conclusion

In this article, the current cooperative control mechanism of FTRHEM in the constant torque and constant power regions is analyzed. On this basis, a full speed current region control strategy is proposed for SP-ac flux regulated FTRHEM. The content is mainly reflected in the following aspects.

1) The accurate mathematical model of FTRHEM is successfully established by constructing the virtual orthogonal vector space through SOGI. Through the comparison and analysis of the measured data of the simulation and experimental platform, it is verified that the model has good consistency in dynamic response characteristics and steady-state accuracy.
2) In the constant torque range, under the proposed current coordinated control strategy, the magnitudes of armature and excitation currents are reduced by 15% and 20%, respectively, compared to the $\varphi = 0°$ control method. Further reductions of 23% and 33% are achieved relative to the $\varphi = 90°$ control method.
3) In the constant power range, the 2D voltage vector constraint domain and the 3D current trajectory envelope surface are innovatively constructed, so that FTRHEM can realize the collaborative optimization of voltage utilization and current in the working range.

References

[1] H. Cao et al., "Generalized active disturbance rejection with reduced-order vector resonant control for PMSM current disturbances suppression," *IEEE Trans. Power Electron.*, vol. 38, no. 5, pp. 6407–6421, May 2023.
[2] Y. Fan, J. Chen, Q. Zhang, and M. Cheng, "An improved inertia disturbance suppression method for PMSM based on disturbance observer and two-degree-of-freedom PI controller," *IEEE Trans. Power Electron.*, vol. 38, no. 3, pp. 3590–3599, Mar. 2023.
[3] T. Wang, L. Guo, K. Wang, J. Wu, C. Liu, and Z. Zhu, "Generalized predictive current control for dual-three-phase PMSM to achieve torque enhancement through harmonic injection," *IEEE Trans. Power Electron.*, vol. 38, no. 5, pp. 6422–6433, May 2023.
[4] R. Jing, G. Zhang, G. Wang, G. Bi, D. Ding, and D. Xu, "An overmodulation strategy based on voltage vector space division for high-speed surface-mounted PMSM drives," *IEEE Trans. Power Electron.*, vol. 37, no. 12, pp. 15370–15381, Dec. 2022.

[5] X. Liu, H. Yang, H. Lin, F. Yu, and Y. Yang, "A novel finite-set sliding-mode model-free predictive current control for PMSM drives without DC-Link voltage sensor," *IEEE Trans. Power Electron.*, vol. 39, no. 1, pp. 320–331, Jan. 2024.

[6] S. Liu, Z. Song, Y. Liu, Y. Chen, and C. Liu, "Flux-Weakening controller design of Dual Three-Phase PMSM drive system with copper loss minimization," *IEEE Trans. Power Electron.*, vol. 38, no. 2, pp. 2351–2363, Feb. 2023.

[7] X. Zhao and S. Niu, "Design of a novel parallel-hybrid-excited Vernier reluctance machine with improved utilization of redundant winding harmonics," *IEEE Trans. Ind. Electron.*, vol. 65, no. 11, pp. 9056–9067, Nov. 2018.

[8] L. Cao, K. T. Chau, C. H. T. Lee, and W.-H. Lam, "Design and analysis of a new parallel-hybrid-excited machine with harmonic-shift structure," *IEEE Trans. Ind. Electron.*, vol. 67, no. 3, pp. 1759–1770, Mar. 2020.

[9] Y. Du, Y. Mao, F. Xiao, X. Zhu, Y. Sun, and L. Quan, "A pole-changing doubly salient permanent magnet motor," *IEEE Trans. Transp. Electrific.*, vol. 8, no. 2, pp. 2479–2489, Jun. 2022.

[10] H. Yi, Y. Fan, Y. Lu, G. Feng, and L. Wei, "MTPA cooperative control strategy of double stator DC-Bias hybrid excitation machine considering inductance nonlinearity," *IEEE Trans. Power Electron.*, vol. 40, no. 5, pp. 7189–7199, May 2025.

[11] Q. Zhang, S. R. Huang, and D. G. Xie, "Design and experimental verification of hybrid excitation machine with isolated magnetic paths," *IEEE Trans. Energy Convers.*, vol. 25, no. 4, pp. 993–1000, Dec. 2010.

[12] J. A. Tapia, F. Leonardi, and T. A. Lipo, "Consequent-pole permanent magnet machine with extended field-weakening capability," *IEEE Trans. Ind. Appl.*, vol. 39, no. 6, pp. 1704–1709, Nov./Dec. 2003.

[13] T. Kosaka, M. Sridharbabu, M. Yamamoto, and N. Matsui, "Design studies on hybrid excitation motor for main spindle drive in machine tools," *IEEE Trans. Ind. Electron.*, vol. 57, no. 11, pp. 3807–3813, Nov. 2010.

[14] D. Wang, D. Zhang, D. Xue, C. Peng, and X. Wang, "A new hybrid excitation permanent magnet machine with an independent AC excitation port," *IEEE Trans. Ind. Electron.*, vol. 66, no. 8, pp. 5872–5882, Aug. 2019.

[15] X. Wang, Y. Fan, Q. Chen, and Z. Wu, "Magnetic circuit feature investigation of a radial–axial brushless hybrid excitation machine for electric vehicles," *IEEE Trans. Transp. Electrific.*, vol. 9, no. 1, pp. 382–393, Mar. 2023.

[16] W. Chen, L. Xu, H. Qiu, C. Yuan, and Q. Wu, "Comprehensive performance comparison of axial-radial hybrid excitation motors with different excitation sources," *IEEE Trans. Energy Convers.*, vol. 40, no. 3, pp. 2436–2445, Sep. 2025, doi: 10.1109/TEC.2025.3543645.

[17] H. Qiu, C. Yuan, W. Chen, X. Ma, and B. Xiong, "Combined regulation performance research of the novel flux-torque regulation hybrid excitation machine with axial-radial magnetic circuit," *IEEE Trans. Transp. Electrific.*, vol. 10, no. 4, pp. 10420–10427, Dec. 2014.

[18] X. Gu, Z. Zhang, L. Sun, S. Yu, W. Zhang, and L. Yu, "Investigation of a parallel hybrid excitation machine with auxiliary winding for loss reduction in flux-weakening operation," *IEEE Trans. Transp. Electrific.*, vol. 10, no. 1, pp. 67–77, Mar. 2024.

[19] N. Pothi, Z. Q. Zhu, and Y. Ren, "Comparison of flux-weakening control strategies of novel hybrid-excited doubly salient synchronous machines," *IEEE Trans. Ind. Appl.*, vol. 55, no. 4, pp. 3589–3597, Jul./Aug. 2019.

[20] W. Ding and S. Li, "Maximum ratio of torque to copper loss control for hybrid excited flux-switching machine in whole speed range," *IEEE Trans. Ind. Electron.*, vol. 66, no. 2, pp. 932–943, Feb. 2019.

[21] Z. Yu, H. Gao, L. Chang, W. Kong, C. Gan, and R. Qu, "MTPA control strategy for six-phase DC-biased hybrid excitation Vernier reluctance machines," in *Proc. IEEE Energy Convers. Congr. Expo.*, 2019, pp. 3807–3812.

[22] B. Wang, D. Wang, X. Wang, G. Xu, and X. Wang, "A maximum torque per copper loss control for AC flux-regulation permanent magnet synchronous motor with magnetic flux co-regulation," *Trans. China Electrotech. Soc.*, vol. 39, no. 12, pp. 3630–3645, Jul. 2024.

[23] X. Wang, Y. Fan, J. Chen, Y. Lei, Q. Chen, and C. H. T. Lee, "The current region control strategy with wide speed range of radial-axial consequent pole hybrid excitation machine for electric vehicles," *IEEE Trans. Transp. Electrific.*, vol. 10, no. 1, pp. 1377–1387, Mar. 2024.

[24] S. Choi and W. J Lee, "Maximum torque per ampere control of a single-phase permanent magnet synchronous motor, Part 1: Maximum torque capability analysis," *J. Elect. Eng. Technol.*, vol. 15, pp. 2617–2625, 2020.

[25] S. Choi and W. J Lee, "Maximum torque per ampere control of a single-phase permanent magnet synchronous motor, Part 2: Variable speed control method," *J. Elect. Eng. Technol.*, vol. 15, pp. 2609–2616, 2020.

[26] X. Liu, D. Niu, Y. Cao, and Q. Zhou, "Position estimation for hybrid excited switched flux PM machine by injecting high-frequency pulse into the field winding," *Trans. China Electrotech. Soc.*, vol. 36, no. 20, pp. 4297–4307, Oct. 2021.

[27] F. Xiao, L. Dong, L. Li, and X. Liao, "A frequency-fixed SOGI-based PLL for single-phase grid-connected converters," *IEEE Trans. Power Electron.*, vol. 32, no. 3, pp. 1713–1719, Mar. 2017.

[28] S. Prakash, J. K. Singh, R. K. Behera, and A. Mondal, "A type-3 modified SOGI-PLL with grid disturbance rejection capability for single-phase grid-tied converters," *IEEE Trans. Ind. Appl.*, vol. 57, no. 4, pp. 4242–4252, Jul./Aug. 2021.